

A laser-engraved wearable sensor for sensitive detection of uric acid and tyrosine in sweat

Yiran Yang^{1,7}, Yu Song^{1,2,7}, Xiangjie Bo^{1,7}, Jihong Min¹, On Shun Pak³, Lailai Zhu⁴, Minqiang Wang¹, Jiabing Tu¹, Adam Kogan¹, Haixia Zhang², Tzung K. Hsiai⁵, Zhaoping Li⁶ and Wei Gao^{1*}

Wearable sweat sensors have the potential to provide continuous measurements of useful biomarkers. However, current sensors cannot accurately detect low analyte concentrations, lack multimodal sensing or are difficult to fabricate at large scale. We report an entirely laser-engraved sensor for simultaneous sweat sampling, chemical sensing and vital-sign monitoring. We demonstrate continuous detection of temperature, respiration rate and low concentrations of uric acid and tyrosine, analytes associated with diseases such as gout and metabolic disorders. We test the performance of the device in both physically trained and untrained subjects under exercise and after a protein-rich diet. We also evaluate its utility for gout monitoring in patients and healthy controls through a purine-rich meal challenge. Levels of uric acid in sweat were higher in patients with gout than in healthy individuals, and a similar trend was observed in serum.

Circulating nutrients and metabolites provide useful indicators of biological processes in the human body, and their concentrations in biofluids have been used for clinical risk assessment, diagnosis, prognosis and monitoring of therapeutic outcomes^{1–4}. Abnormal concentrations of circulating metabolites and nutrients are associated with health conditions such as metabolic syndrome and cardiovascular disease. Wearable devices^{5–14}, such as wearable sweat sensors^{15–23}, have the potential to capture changes in health rapidly, continuously and non-invasively. For example, chloride concentration in sweat is the gold standard to diagnose cystic fibrosis²⁰, and glucose concentration in sweat is being intensively explored for diabetes management^{16,20,24}.

Current wearable sweat sensors are primarily focused on a limited number of electrolytes and metabolites monitored via ion-selective sensors or enzymatic electrodes^{18,19,25}. Among the analytes for which wearable sensors do not exist are uric acid (UA) and tyrosine (Tyr). UA is a risk factor for cardiovascular disease^{26,27}, type 2 diabetes^{28,29} and renal disease³⁰, and has been widely used in clinical settings for the management of gout^{31–33}, the most common inflammatory arthritis affecting tens of millions of people worldwide³⁴. Tyr is a conditionally essential amino acid involved in brain signaling and in the production of dopamine and stress hormones (for example, noradrenaline and adrenaline)³⁵. Abnormal Tyr concentrations are linked to metabolic disorders such as tyrosinemia^{36,37}, liver diseases³⁷, neuropsychiatric and eating disorders^{38,39}. Measurement of serum UA and Tyr is well established for metabolic and nutritional management^{1,28,31,38}. However, studies on sweat UA and Tyr are scarce^{40,41}, and their use for dynamic health monitoring and personalized intervention has not been investigated. Measurement of UA and Tyr in sweat is challenging because of their low concentrations.

We designed our sensor to address the main technological challenges. Microfluidics is essential for on-body sweat sampling to minimize sweat contamination and evaporation from the skin and to provide high temporal resolution of sweat dynamics^{19,42,43}.

Most reported wearable microfluidic platforms are based on silicone elastomers, which require complicated fabrication processes and expensive microfabrication facilities^{5,15–17}. Considering that scalable manufacture is crucial for widespread implementation of wearable sensors, a promising fabrication technology is CO₂ laser engraving, which may allow rapid engraving of patterns in ambient conditions and reduce personnel training and process optimization. Multimodal sensing of molecular analytes and vital signs provides a more comprehensive perspective on physiological conditions^{15,44}, but the incorporation of both chemical sensing and physical sensing onto a wearable device remains challenging. This process usually requires integration of different materials and layers, which may hamper the wearability and sensing accuracy of the device. The use of CO₂ laser-engraving technology has not been used to fabricate a multimodal wearable system.

Our sweat sensor is entirely laser engraved to facilitate scalable manufacture and flexibility for the wearer's comfort. It enables wireless continuous monitoring of UA, Tyr and vital signs (Fig. 1a). It consists of a highly sensitive laser-engraved graphene-based chemical sensor (LEG-CS) for monitoring low concentrations of UA and Tyr, multiplexed LEG-based physical sensors (LEG-PS) for monitoring temperature and respiration rate and a laser-engraved multi-inlet microfluidic module for dynamic sweat sampling. We validated the system against gold-standard assays and in physically trained and untrained subjects and evaluated its potential for monitoring gout.

Results

Design of the entirely laser-engraved sensor for multimodal monitoring. A CO₂ laser-cutting machine is used to fabricate all key components of the sensor: the LEG-CS, the LEG-PS and the multi-inlet microfluidic module (Fig. 1a). The system contains five layers, including multiplexed sensors scribed on a polyimide substrate, microfluidic channels patterned on a double-sided medical

¹Andrew and Peggy Cherng Department of Medical Engineering, California Institute of Technology, Pasadena, CA, USA. ²National Key Lab of Micro/Nano Fabrication Technology, Peking University, Beijing, China. ³Department of Mechanical Engineering, Santa Clara University, Santa Clara, CA, USA.

⁴Department of Mechanical and Aerospace Engineering, Princeton University, Princeton, NJ, USA. ⁵Division of Cardiology, Department of Medicine, David Geffen School of Medicine, University of California, Los Angeles, CA, USA. ⁶Division of Clinical Nutrition, Department of Medicine, David Geffen School of Medicine, University of California, Los Angeles, CA, USA. ⁷These authors contributed equally: Yiran Yang, Yu Song, Xiangjie Bo. *e-mail: weigao@caltech.edu

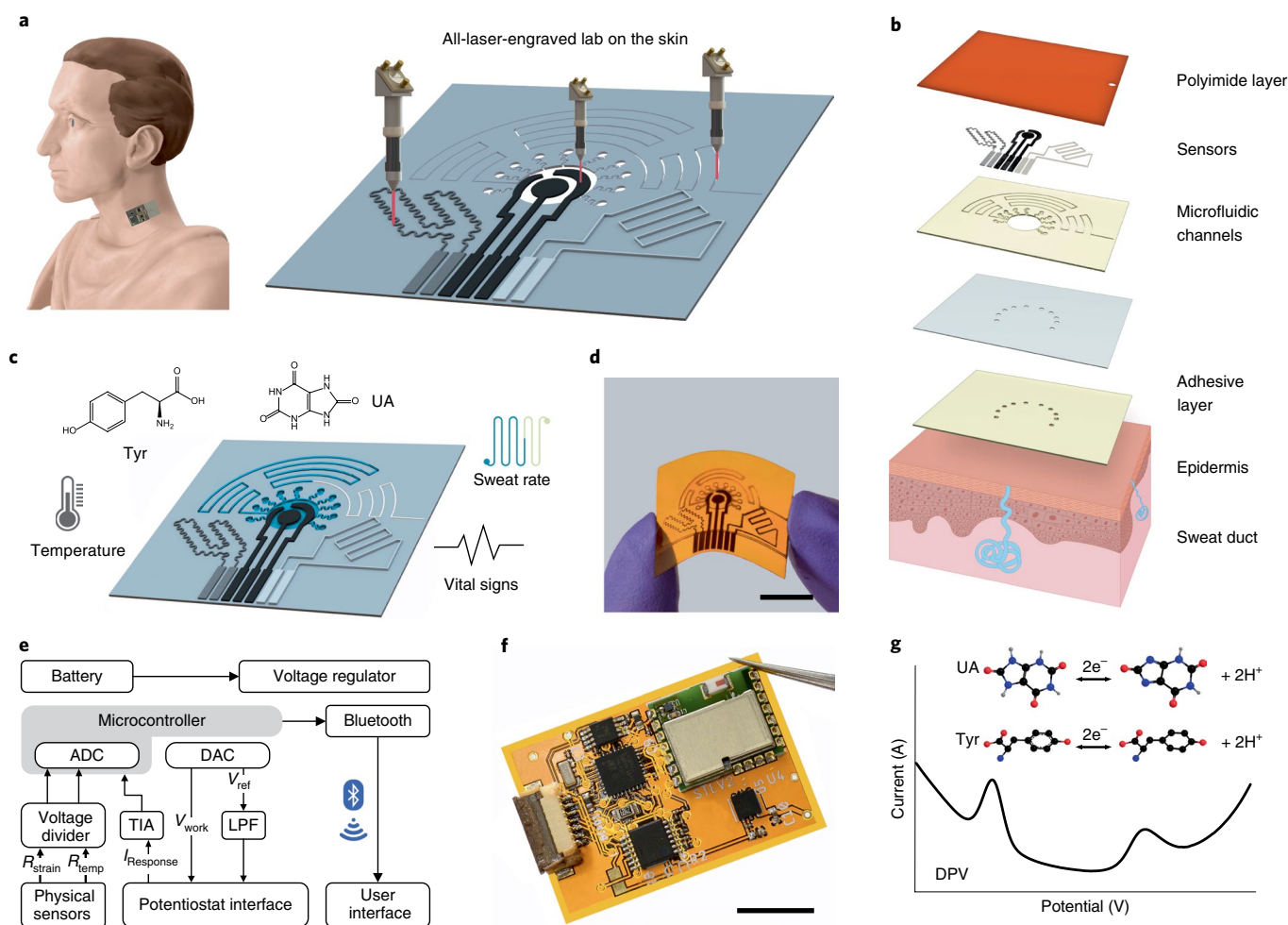


Fig. 1 | Schematics of the sweat sensor for metabolic and nutritional management. **a**, The sensor with entirely laser-engraved components: the microfluidic module and the LEG-based chemical and physical sensors. **b**, Layers of the sensor, from the bottom layer in contact with epidermis to the top layer. **c**, Multiple functions of the sensor: ultrasensitive sweat UA and Tyr detection, sweat rate estimation, temperature sensing and vital-sign (for example, heart rate and respiration rate) monitoring. **d**, Photographic image of a flexible lab-on-skin patch. Scale bar, 1 cm. **e**, System-level block diagram showing the signal transduction, processing and wireless transmission from the sensors to the user interface. DAC, digital-to-analog converter. **f**, Photographic image of the FPCB. Scale bar, 1 cm. **g**, Detection of UA and Tyr with DPV in which analyte level is determined from the oxidation peak height.

adhesive and inlet-engraved polyethylene terephthalate (PET) and medical adhesive layers (Fig. 1b and Supplementary Fig. 1). As sweat flows into the system, the LEG-CS measures the dynamics of sweat UA and Tyr while the LEG-PS measures skin temperature and strain-related physiological patterns (for example, respiration rate or heart rate) continuously (Fig. 1c,d). In addition, sweat loss and sweat rate can be obtained with the circular patterns of microfluidic channels. Two laser-engraving modes are used: raster mode is utilized for chemical sensors while vector mode is used for microfluidic patterns and physical sensors (Supplementary Figs. 2 and 3). Such multimodal microfluidic sensor patches can be prepared at a large scale (Supplementary Fig. 4). The resulting LEG structures are characterized using Raman and X-ray photoelectron spectroscopies (Supplementary Figs. 5 and 6). The disposable patch is connected to a reusable flexible printed circuit board (FPCB) (Fig. 1d–f). The system-level block diagram in Fig. 1e and the circuit diagram in Supplementary Fig. 7 illustrate the flow of electrical signals in the electrochemical and physical sensor measurements. For chemical sensing, the preprogrammed microcontroller generates the desired stimulation waveform (smoothed by an analog low-pass filter) to apply a specific sensing voltammogram on the electrodes through an external digital-to-analog converter. The resulting current

response is amplified and converted to voltage by a transimpedance amplifier (TIA) and read by an analog-to-digital converter (ADC). Differential pulse voltammetry (DPV) is chosen here to evaluate ultralow-level sweat UA and Tyr on the basis of the amplitude of the oxidation current peak (Fig. 1g). The responses of the physical sensors are acquired through voltage dividers and the ADC. The acquired data are wirelessly transmitted to the user device over Bluetooth for further analysis.

Characterization of the LEG-based UA and Tyr sensor. Owing to its unique electrochemical properties arising from the fast electron mobility, high current density and ultralarge surface area, graphene is an appropriate candidate for building high-performance sensors to detect ultralow levels of electroactive analytes in body fluids. Laser cutting has been used to directly obtain graphene structures from a variety of substrates toward energy storage and fluid capture applications^{45–47}. Here we manufactured highly sensitive LEG-CS on polyimide via raster mode (Fig. 2a–d and Supplementary Fig. 2). The three-electrode LEG-CS could selectively catalyze the oxidation of UA and Tyr at specific potentials (Fig. 2b). After optimization on the basis of the DPV peak amplitudes of UA and Tyr in the standard solutions (Supplementary Fig. 8 and Supplementary Table 1)

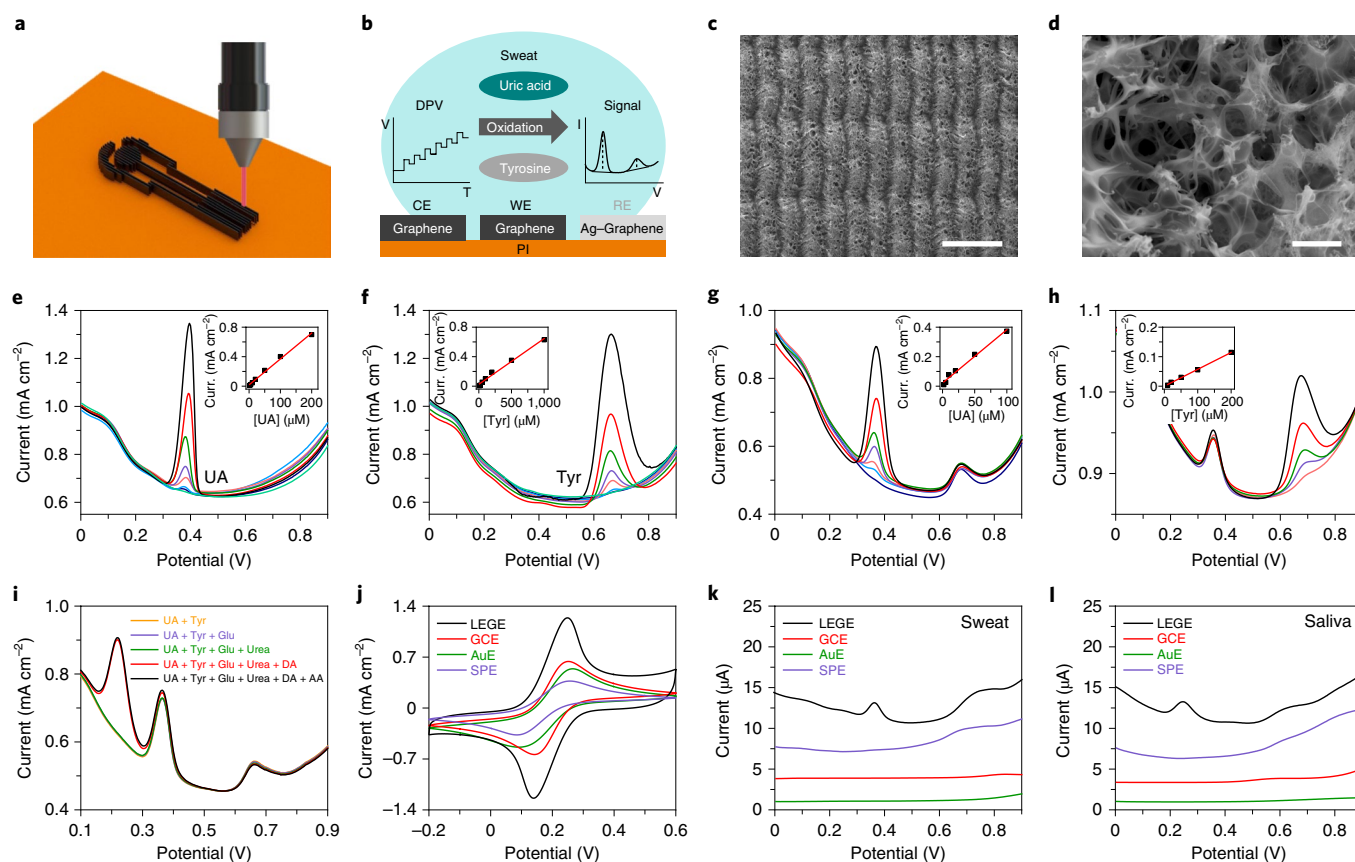


Fig. 2 | Schematics and characterization of the LEG-based UA and Tyr sensor. **a**, Schematic of the raster mode for LEG-CS fabrication. **b**, A three-electrode LEG-based flexible sensor for simultaneous UA and Tyr detection. CE, counter electrode; WE, working electrode; RE, reference electrode. **c, d**, SEM images of the LEG-CS. Scale bars, 200 μm (**c**) and 3 μm (**d**). **e, f**, UA (**e**) and Tyr (**f**) detection with the LEG-CS in a 0.01M ABS solution. Insets are the corresponding calibration plots. Curr., current. **g, h**, Simultaneous and selective detection of UA in the presence of 50 μM Tyr (**g**) and Tyr in the presence of 50 μM UA (**h**). **i**, Simultaneous detection of 50 μM UA and 50 μM Tyr in the presence of common interferences: 170 μM glucose (Glu), 10 mM urea, 25 μM dopamine (DA) and 50 μM ascorbic acid (AA). **j**, Cyclic voltammery scans of an LEG electrode (LEGE), a glassy carbon electrode (GCE), a gold electrode (AuE), and a screen-printed carbon electrode (SPE) in a solution containing 5 mM $[\text{Fe}(\text{CN})_6]^{3-}$ and 0.2 M KCl. **k, l**, DPV signals in raw sweat (**k**) and saliva (**l**) samples from an LEG electrode, a glassy carbon electrode, a gold electrode and a screen-printed carbon electrode. Experiments in **e–l** were repeated five times independently with similar results.

and electrochemical impedance spectroscopy (Supplementary Fig. 9), the electrocatalytic activity and reproducibility of LEG-CS for direct oxidation of UA and Tyr at physiological concentrations had sensitivities of $3.50 \mu\text{A} \mu\text{M}^{-1} \text{cm}^{-2}$ and $0.61 \mu\text{A} \mu\text{M}^{-1} \text{cm}^{-2}$, and low detection limits of $0.74 \mu\text{M}$ and $3.6 \mu\text{M}$, respectively (Fig. 2e,f and Supplementary Fig. 10). Two distinct current peaks at $\sim 0.39 \text{ V}$ and $\sim 0.64 \text{ V}$ from the DPV scans correspond to the oxidation reactions of UA and Tyr, respectively. The LEG-based UA and Tyr sensor shows excellent selectivity over other analytes in sweat at physiologically relevant concentrations⁴⁸ (Fig. 2g–i, Supplementary Note 1, Supplementary Table 2 and Supplementary Figs. 11–15). The LEG-CS displays superior electrochemical performance over commercial glassy carbon, screen-printed carbon and gold electrodes (Fig. 2j). Moreover, it enables direct detection of UA and Tyr in raw body fluids (that is, sweat and saliva) (Fig. 2k,l). The response of UA and Tyr sensing can be wirelessly recorded using the as-designed FPCB (Supplementary Figs. 16 and 17). Although we focus on detection of UA and Tyr in this work, LEG-CS is able to detect ultralow levels of other electroactive molecules such as ascorbic acid and dopamine (Supplementary Fig. 18). The LEG-CS is mechanically flexible, fully compliant with the skin and exhibits mechanical and electrochemical stability (Supplementary Fig. 19).

Design and characterization of the LEG-based vital-sign monitor. The LEG has unique properties for designing resistive physical sensors: as the temperature rises, its conductivity increases owing to increased electron–phonon scattering and thermal velocity of electrons in the sandwiched layers⁴⁹ (Fig. 3a); when an external strain is applied, its three-dimensional porous structure is compressed, resulting in decreased resistance (Fig. 3b). Here the LEG-based temperature and piezoresistive strain sensors are fabricated in vector mode (Fig. 3c,d and Supplementary Fig. 2). Both material morphology and sensor layout are important in achieving the desired sensor performance: the fiber-like structure resulted from a high dose of local laser power (Fig. 3d and Supplementary Fig. 20) coupled with a straight-line design (strain sensor) yields the highest strain response; the compact structure (Fig. 3c) coupled with serpentine line design (temperature sensor) is less susceptible to strain variations (Fig. 3e). The temperature sensor shows a fast, accurate and stable response to temperature variations with a sensitivity of $-0.06\% \text{ } ^\circ\text{C}^{-1}$ and a low detection limit of $0.051 \text{ } ^\circ\text{C}$ (Fig. 3f–h and Supplementary Fig. 21), which indicates the negative temperature coefficient behavior of the LEG. The strain sensor is fabricated at a low laser speed for large strain response and high stability (Fig. 3i,j and Supplementary Fig. 22), which is ideally suited for accurate monitoring of respiration rate (Fig. 3k) and heart rate (Supplementary Fig. 23), as

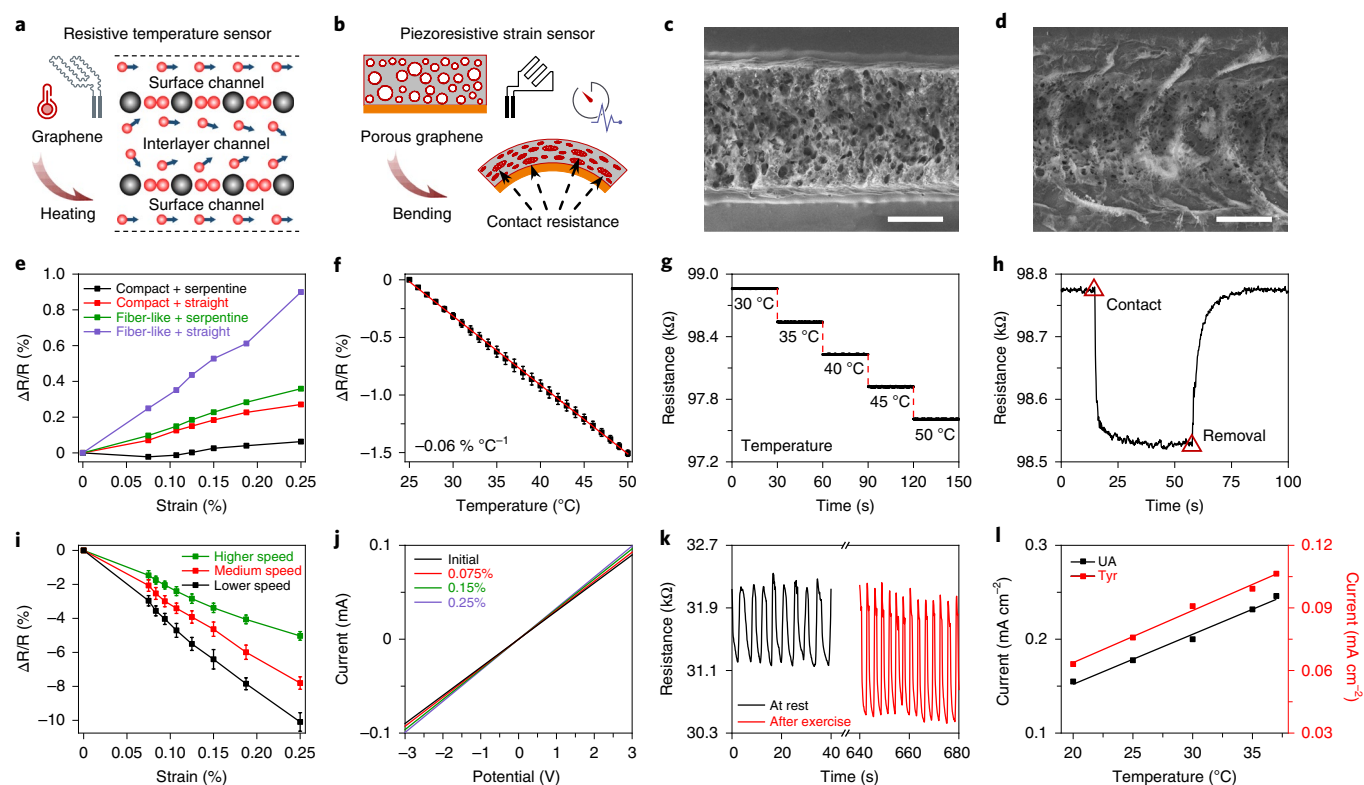


Fig. 3 | Design and characterization of the LEG-based vital-sign sensors. **a, b**, Mechanisms of temperature sensing (**a**) and strain sensing (**b**) using LEG. **c, d**, SEM images of an LEG-based temperature sensor (**c**) and an LEG-based strain sensor (**d**). Scale bars, 100 μm . **e**, Strain responses of LEG with different morphologies and layouts. **f, g**, Calibration plot (**f**) and dynamic response (**g**) of the LEG-based temperature sensor in the physiological temperature range. Error bars represent the s.d. from ten sensors of different batches (ten measurements per sensor). **h**, Dynamic response of an LEG-based temperature sensor upon contact with and removal from the human body. **i**, Strain responses of the LEG-based strain sensors prepared with varied laser scanning speeds. Error bars represent the s.d. from ten sensors of different batches (ten measurements per sensor). **j**, I - V curves of a strain sensor under different strains. **k**, Real-time respiration rate measurement with a strain sensor, at rest and after exercise. **l**, Dependence of the response of LEG-CS on the temperature. Condition, 50 μM UA and 100 μM Tyr in ABS. $\Delta R/R$ represents the ratio of the resistance change to the flat state resistance of the vital-sign sensor at 25 $^{\circ}\text{C}$. Experiments in **e** and **g** were repeated ten times independently with similar results. Experiments in **h** and **j-l** were repeated five times independently with similar results.

validated with commercial vital monitors (Supplementary Fig. 24). After 10,000 bending cycles, the flat-state resistance of the strain sensor remains stable (Supplementary Fig. 25). The temperature and strain sensor response can be accurately monitored by the FPCB (Supplementary Fig. 26). Considering that the response of the UA and Tyr sensor can be influenced by temperature variations (Fig. 3l), the temperature sensor readings could be used for real-time chemical sensor calibration during on-body use.

Design and performance characterization of the laser-engraved microfluidics. Laser engraving enables rapid bulk manufacturing of microfluidic devices⁵⁰. The microfluidic module is fabricated in vector mode to fully cut through double-sided adhesives (Fig. 4a,b). The use of microfluidics enhanced the sweat sampling process and achieved higher temporal resolution for wearable sensing by constantly supplying newly secreted sweat to the sensor. In response to inflow of solutions at a new solute concentration, the time taken for the solute concentration in the reservoir to adjust to the new concentration (referred to as the refreshing time hereafter) is a key performance indicator of the microfluidic module. We used numerical simulations to determine the effects of the inlet number and flow rates on the refreshing time (Fig. 4c,d). For the case of ten inlets, with an experimentally measured sweat rate (1.5 $\mu\text{l min}^{-1}$) as the inlet flow rate, the refreshing time taken to reach 90% of the new solute concentration was around 2.5 min, for a change of solute

concentration from 20 μM to 80 μM (Fig. 4e). During the on-body trials, the microfluidic patch effectively sampled sweat with high temporal resolution (Fig. 4f and Supplementary Fig. 27). Moreover, it monitored sweat rate or sweat loss on different body parts through optical image analysis¹⁹ (Supplementary Fig. 28; Methods). Wireless and continuous sensing capabilities of the microfluidic-based sensor are performed via continuous analyte solution injection at physiological sweat rates (Fig. 4g-i). The sensor patch reliably and continuously measured the UA and Tyr levels ($\pm 0.49\%$ and $\pm 1.07\%$, respectively) through successive DPV scans over a 15-cycle period (Fig. 4h and Supplementary Fig. 29a). When the input solution was switched from 20 to 80 μM for UA and from 50 to 200 μM for Tyr, the patch took less than 3 min to reach a new stable reading with a hysteresis of ~ 1 min (Fig. 4i and Supplementary Fig. 29b), indicating the high temporal resolution of the microfluidic sensing system. As illustrated in Supplementary Fig. 30, with a 45-s scan cycle every 2.5 min, the microfluidic system showed very stable readings for UA and Tyr sensing during five successive scans ($\pm 1.25\%$ and $\pm 3.24\%$, respectively) even when the flow rate was as small as 0.25 $\mu\text{l min}^{-1}$, indicating that the molecular depletion in the confined reservoir during DPV scans will not affect the sensing accuracy.

In vivo system validation of the wearable sensor. The fully integrated system could be comfortably worn on different body parts (Fig. 5a). Real-time measurement of sweat UA and Tyr, respiration

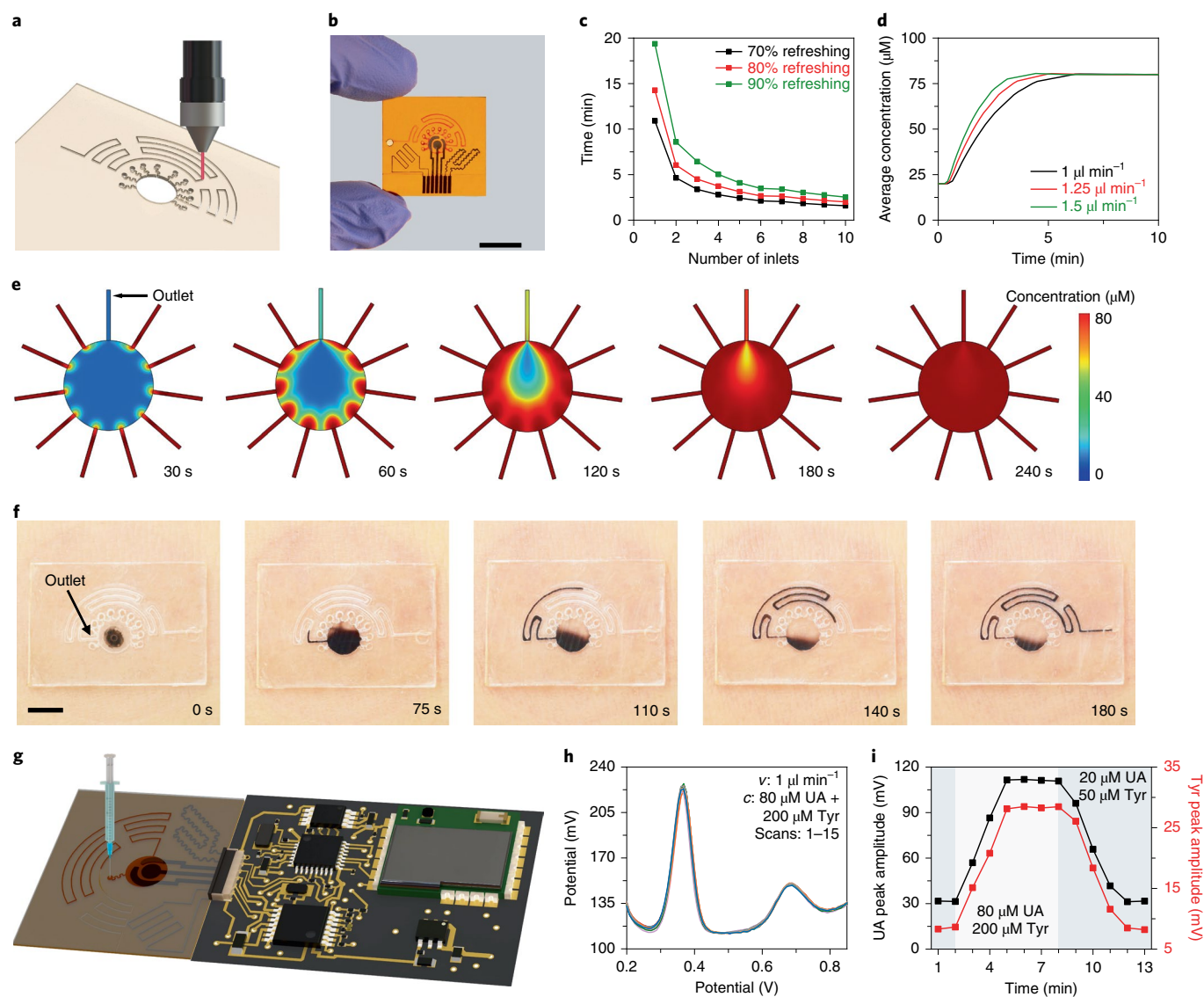


Fig. 4 | Design and characterization of the microfluidic system. **a**, Schematic of vector-mode laser cutting for microfluidic fabrication. **b**, Photographic image of the microfluidic channels. Scale bar, 1 cm. **c**, Numerical simulation of the refreshing time required for the average concentration to reach 70%, 80% and 90% of the new solute concentration (that is, from 20 μM UA to 80 μM UA). Flow rate for each inlet, 0.15 $\mu\text{l min}^{-1}$. **d**, Simulations of the time evolution of the average concentration at different total inlet flow rates. **e**, Simulations of the distributions of solute concentration over the bottom surface of the reservoir at different time instances (inlet flow rate, 1.5 $\mu\text{l min}^{-1}$). **f**, Photographic images of the microfluidic sweat sampling during an iontophoresis-induced sweat secretion process. Scale bar, 5 mm. **g**, Setup of the flow test to wirelessly monitor the analyte levels. A syringe pump is used to inject analyte solutions through an inlet. **h**, Successive DPV scans of 15 cycles in 80 μM UA and 200 μM Tyr with a fixed flow rate of 1 $\mu\text{l min}^{-1}$. The experiment was repeated three times independently with similar results. **i**, Dynamic and wireless UA sensing before and after switching the input UA and Tyr concentration from 20 and 50 μM , to 80 and 200 μM , respectively.

rate and temperature from the neck of a healthy individual in a controlled cycling exercise was demonstrated (Fig. 5b and Supplementary Fig. 31). The temperature increased initially and stabilized after 600 s and the respiration rate (obtained via fast Fourier transform as shown in Supplementary Fig. 32) followed similar trends. On the other hand, a decreased trend in sweat UA and Tyr concentrations was observed, which is likely attributable to profuse sweat secretion⁴⁰. Varied UA and Tyr secretion at different locations was observed (Fig. 5c,d and Supplementary Fig. 33). We determined the accuracy of the wearable sensor for analyzing raw sweat samples using high-performance liquid chromatography (HPLC) and commercial colorimetric assay kits (Fig. 5e,f, Supplementary Tables 3 and 4, and Supplementary Figs. 34–36) and obtained high Pearson correlation coefficients of 0.963 and 0.965

for UA and Tyr sensing, respectively, suggesting the reliability of the sensor measurements.

Considering that sweat Tyr may be related to fitness condition⁴¹, we carried out controlled human performance trials on five physically untrained and five trained subjects (athletes) to validate the system (Fig. 5g,h). As expected, we observed lower sweat Tyr concentrations in trained athlete subjects (Fig. 5h). The sensor patch was able to dynamically monitor the Tyr intake and supplementation, as well as metabolism (Supplementary Fig. 37). As both tyrosine and uric acid are metabolic products of protein diets, system validations toward nutritional and metabolic monitoring were performed through a protein intake study on three healthy individuals. Higher levels of both sweat UA and Tyr were observed in all the subjects after a high-protein diet (Supplementary Fig. 38).

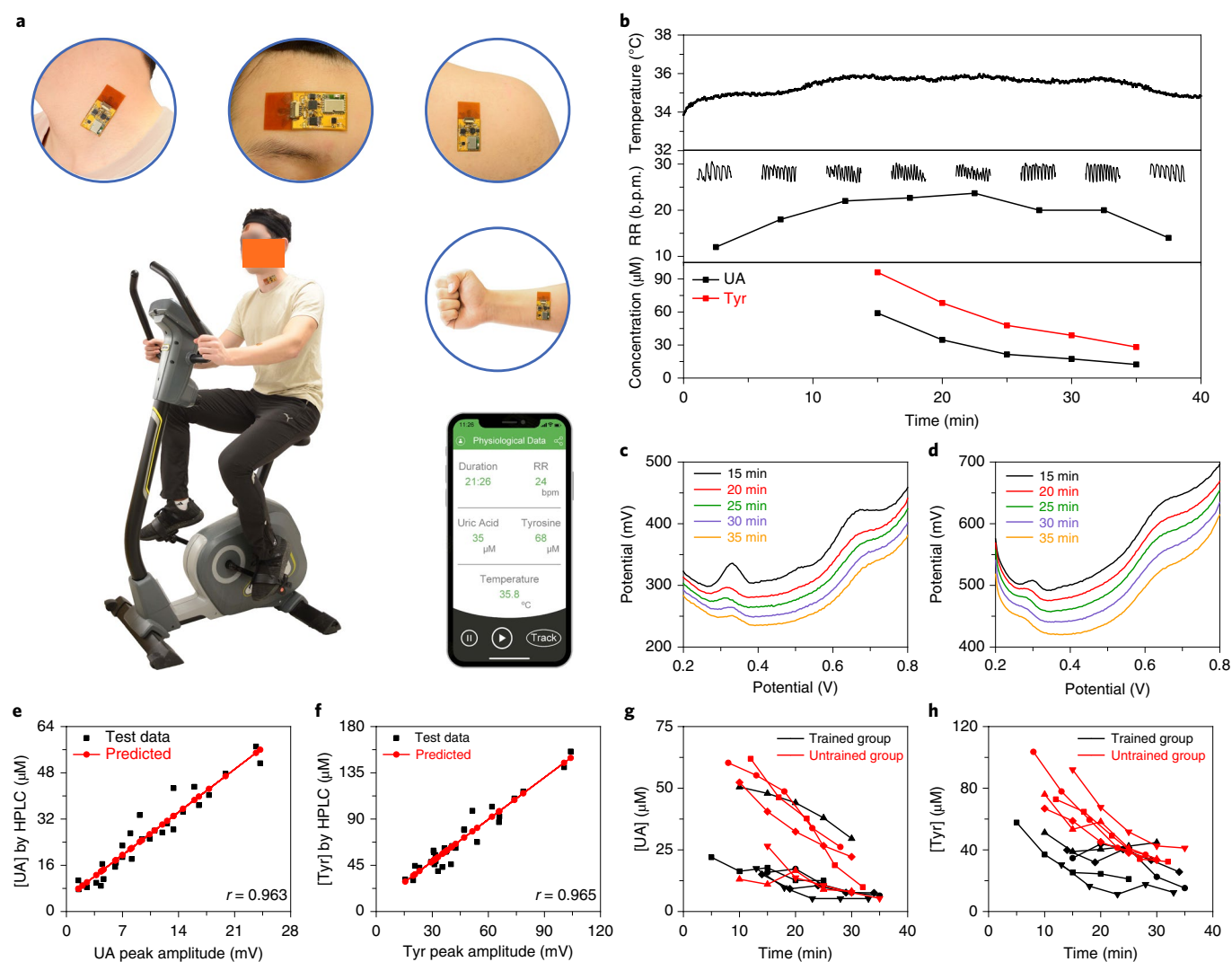


Fig. 5 | In vivo system validation of the lab on the skin. **a**, Photographs of a healthy subject wearing the sensor patch at different body parts. **b**, Real-time, continuous in situ measurement of respiration rate (RR; measured in breaths per minute (b.p.m.)), temperature and sweat UA and Tyr levels from the neck of a healthy subject during a constant-load stationary cycling exercise, which includes a 5-min warm-up, 30-min constant-load cycling and 5-min cool-down. Insets in the respiration rate plot illustrate 30-s strain sensor signals recorded at 5-min intervals. **c,d**, DPV curves obtained during the on-body UA and Tyr measurement from the neck (**c**) and the forehead (**d**). **e,f**, Validation of the LEG-CS for analyzing UA (**e**) and Tyr (**f**) in raw sweat samples using HPLC analysis. The data are based on 29 sweat samples collected from healthy human subjects. The Pearson correlation coefficient was acquired through linear regression. **g,h**, Dynamics monitoring of sweat UA (**g**) and Tyr (**h**) in physically trained and untrained subjects during controlled cycling exercises.

Evaluation of the wearable sensor for non-invasive gout management. The global burden of gout is increasing³⁴. Gout is often characterized by chronic hyperuricemia, an elevated UA level exceeding the physiological saturation threshold³¹. Many risk factors, such as an increased intake of dietary purines and alcohol³³, can lead to gout attacks (Fig. 6a). Monitoring serum UA is important in personalized gout treatment and management (for example, urate-lowering therapy, flare-up preventions and dietary or nutritional control)³¹. To evaluate our sensor for gout management, we performed a controlled purine-diet study in healthy male and female subjects. For subjects with overnight fasting ($n=6$), both serum and sweat UA levels increased after a purine-rich diet (Fig. 6b–e and Supplementary Figs. 39). The subsequent human study, carried out 2 h after a regular lunch, indicated that higher sweat UA levels were identified from the subjects with hyperuricemia ($n=4$) and patients with gout (without medication, $n=6$) than from the healthy subjects ($n=5$), with a similar trend in serum UA levels (Fig. 6f and validated in Supplementary Fig. 40 with HPLC). This

approach also shows promise for personalized dosage adjustment in urate-lowering therapy, as illustrated in Supplementary Fig. 41. The dynamic changes of sweat UA before and after a purine-rich diet over a 7-h period measured by the wearable sensor (Fig. 6g) closely resembled those of serum UA. We obtained a high correlation coefficient of 0.864 between sweat and serum UA concentrations (Fig. 6h), suggesting the potential use of sweat UA as a biomarker for gout management.

Discussion

Given the rich physiological information present in human sweat, the transition from traditional blood analysis to in situ sweat analysis using wearable sensors could provide a non-invasive, continuous means to monitor metabolites and to guide personalized nutritional and metabolic management. However, current wearable sweat sensors face several major challenges: (1) the lack of available highly sensitive wearable sensors that can monitor sweat analytes beyond a few electrolytes and metabolites via ion-selective or enzymatic

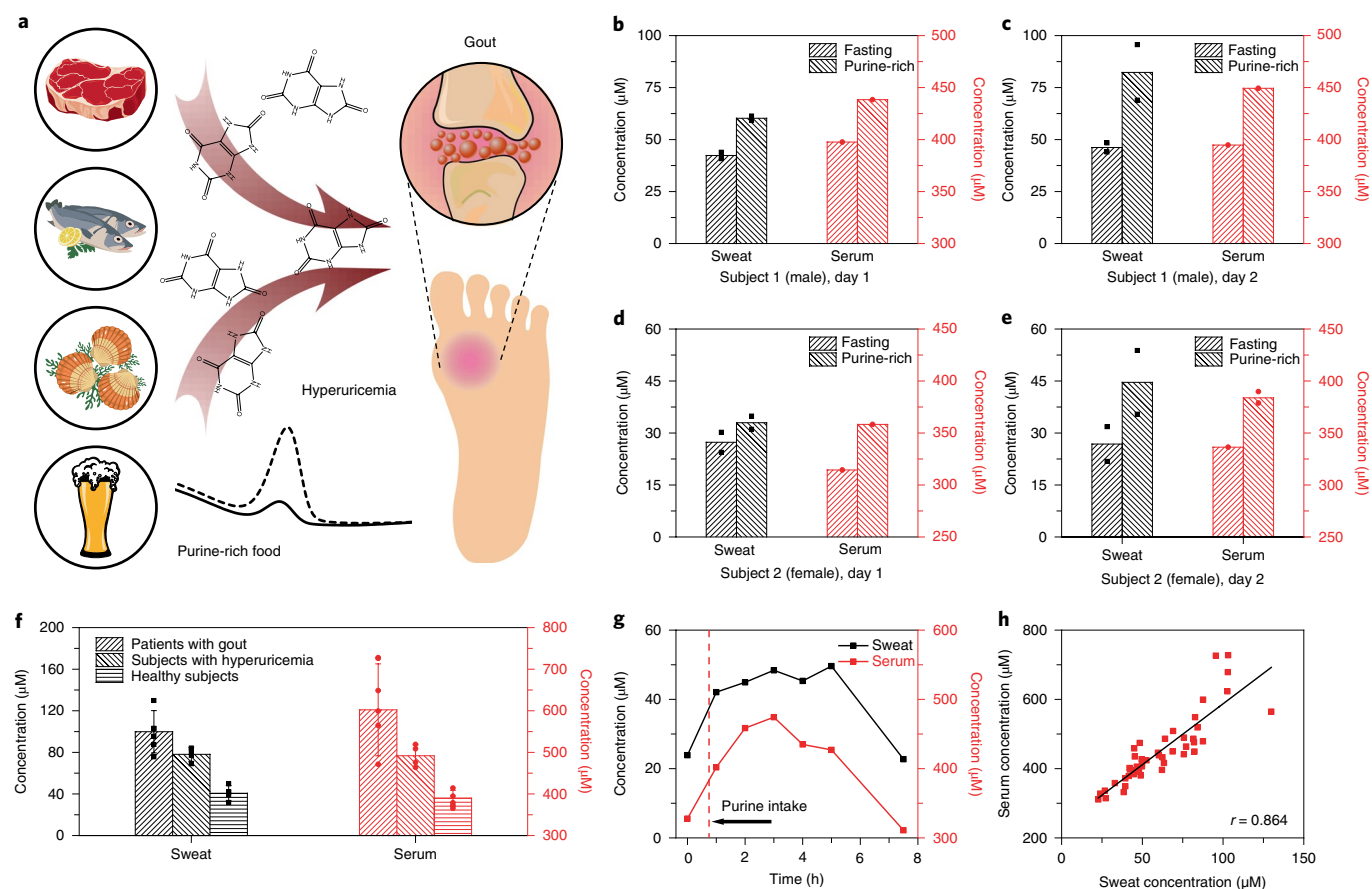


Fig. 6 | Non-invasive gout management using the sweat sensor. **a**, Purine-rich diets increase the risk of gout attacks. **b–e**, UA levels in sweat and serum of a healthy male (**b,c**) and a healthy female (**d,e**) subject under fasting condition, and after a purine-rich diet on two different days. Bars in **b–e** indicate the mean value of the first two successive measurements. **f**, The sweat and serum UA levels obtained using the wearable sensors in patients with diagnosed gout, subjects with hyperuricemia and healthy individuals. Bars indicate the mean value of each category; error bars represent the s.d. of measurements from all the subjects in each category ($n=6$ for patients with gout, $n=4$ for subjects with hyperuricemia and $n=5$ for healthy subjects). **g**, Dynamic changes of sweat and serum UA from one healthy subject before and after a purine-rich diet over a 7-h period. The experiment was repeated twice independently with similar results. **h**, The correlation of sweat and serum UA concentrations from the human studies. The Pearson correlation coefficient was acquired through linear regression ($n=46$ biologically independent samples).

sensors; (2) the low in situ sensing accuracy owing to factors such as skin contamination, sweat evaporation and long refreshing time; and (3) the lack of correlation study between the sweat analyte level and a particular health condition.

Our laser-engraved multimodal sensor enables efficient microfluidic sweat sampling, sensitive molecular sensing and multiplexed vital-sign sensing. Owing to its fast electron mobility, high current density and ultralarge surface area, the graphene-based chemical sensor achieves rapid and accurate detection of UA and Tyr in human sweat in situ. Moreover, its manufacture is likely scalable as all three key modules (physical sensors, chemical sensors, and microfluidic module) are fabricated with a widely available CO₂ laser engraving approach. We have demonstrated sweat UA and Tyr detection using a wearable system and correlated our results with serum measurements in both healthy subjects and patients with gout. The high correlation coefficient obtained in our small pilot study indicates the promise of this approach for personalized monitoring of UA levels. Further studies may also assess its value in non-invasive monitoring of gout, cardiovascular disease, type 2 diabetes and renal disease.

Online content

Any methods, additional references, Nature Research reporting summaries, source data, extended data, supplementary information,

acknowledgements, peer review information; details of author contributions and competing interests; and statements of data and code availability are available at <https://doi.org/10.1038/s41587-019-0321-x>.

Received: 2 May 2019; Accepted: 23 October 2019;

Published online: 25 November 2019

References

- Wang, T. J. et al. Metabolite profiles and the risk of developing diabetes. *Nat. Med.* **17**, 448–453 (2011).
- Suhre, K. et al. Human metabolic individuality in biomedical and pharmaceutical research. *Nature* **477**, 54–60 (2011).
- Illig, T. et al. A genome-wide perspective of genetic variation in human metabolism. *Nat. Genet.* **42**, 137–141 (2010).
- Wu, G. Amino acids: metabolism, functions, and nutrition. *Amino Acids* **37**, 1–17 (2009).
- Kim, D. H. et al. Epidermal electronics. *Science* **333**, 838–843 (2011).
- Someya, T., Bao, Z. & Malliaras, G. G. The rise of plastic bioelectronics. *Nature* **540**, 379–385 (2016).
- Kim, J., Campbell, A. S., de Avila, B. E. & Wang, J. Wearable biosensors for healthcare monitoring. *Nat. Biotechnol.* **37**, 389–406 (2019).
- Heikenfeld, J. et al. Wearable sensors: modalities, challenges, and prospects. *Lab Chip* **18**, 217–248 (2018).
- Park, S. et al. Self-powered ultra-flexible electronics via nano-grating-patterned organic photovoltaics. *Nature* **561**, 516–521 (2018).

10. Son, D. et al. An integrated self-healable electronic skin system fabricated via dynamic reconstruction of a nanostructured conducting network. *Nat. Nanotechnol.* **13**, 1057–1065 (2018).
11. Wang, C. et al. Monitoring of the central blood pressure waveform via a conformal ultrasonic device. *Nat. Biomed. Eng.* **2**, 687–695 (2018).
12. Hua, Q. et al. Skin-inspired highly stretchable and conformable matrix networks for multifunctional sensing. *Nat. Commun.* **9**, 244 (2018).
13. Wang, C. et al. User-interactive electronic skin for instantaneous pressure visualization. *Nat. Mater.* **12**, 899–904 (2013).
14. Yang, Y. & Gao, W. Wearable and flexible electronics for continuous molecular monitoring. *Chem. Soc. Rev.* **48**, 1465–1491 (2019).
15. Gao, W. et al. Fully integrated wearable sensor arrays for multiplexed in situ perspiration analysis. *Nature* **529**, 509–514 (2016).
16. Lee, H. et al. A graphene-based electrochemical device with thermoresponsive microneedles for diabetes monitoring and therapy. *Nat. Nanotechnol.* **11**, 566–572 (2016).
17. Koh, A. et al. A soft, wearable microfluidic device for the capture, storage, and colorimetric sensing of sweat. *Sci. Transl. Med.* **8**, 366ra165 (2016).
18. Bariya, M., Nyein, H. Y. Y. & Javey, A. Wearable sweat sensors. *Nat. Electron.* **1**, 160–171 (2018).
19. Choi, J., Ghaffari, R., Baker, L. B. & Rogers, J. A. Skin-interfaced systems for sweat collection and analytics. *Sci. Adv.* **4**, eaar3921 (2018).
20. Emaminejad, S. et al. Autonomous sweat extraction and analysis applied to cystic fibrosis and glucose monitoring using a fully integrated wearable platform. *Proc. Natl Acad. Sci. USA* **114**, 4625–4630 (2017).
21. Bandonkar, A. J. et al. Battery-free, skin-interfaced microfluidic/electronic systems for simultaneous electrochemical, colorimetric, and volumetric analysis of sweat. *Sci. Adv.* **5**, eaav3294 (2019).
22. Nakata, S. et al. A wearable pH sensor with high sensitivity based on a flexible charge-coupled device. *Nat. Electron.* **1**, 596–603 (2018).
23. Heikenfeld, J. et al. Accessing analytes in biofluids for peripheral biochemical monitoring. *Nat. Biotechnol.* **37**, 407–419 (2019).
24. Lee, H. et al. Wearable/disposable sweat-based glucose monitoring device with multistage transdermal drug delivery module. *Sci. Adv.* **3**, e1601314 (2017).
25. Jia, W. et al. Electrochemical tattoo biosensors for real-time noninvasive lactate monitoring in human perspiration. *Anal. Chem.* **85**, 6553–6560 (2013).
26. Feig, D. I., Kang, D. H. & Johnson, R. J. Uric acid and cardiovascular risk. *N. Engl. J. Med.* **359**, 1811–1821 (2008).
27. Gagliardi, A. C., Miname, M. H. & Santos, R. D. Uric acid: A marker of increased cardiovascular risk. *Atherosclerosis* **202**, 11–17 (2009).
28. Bhole, V., Choi, J. W., Kim, S. W., de Vera, M. & Choi, H. Serum uric acid levels and the risk of type 2 diabetes: a prospective study. *Am. J. Med.* **123**, 957–961 (2010).
29. Kodama, S. et al. Association between serum uric acid and development of type 2 diabetes. *Diabetes Care* **32**, 1737–1742 (2009).
30. Kohagura, K. et al. An association between uric acid levels and renal arteriopathy in chronic kidney disease: a biopsy-based study. *Hypertens. Res.* **36**, 43–49 (2013).
31. Terkeltaub, R. Update on gout: new therapeutic strategies and options. *Nat. Rev. Rheumatol.* **6**, 30–38 (2010).
32. Major, T. J., Dalbeth, N., Stahl, E. A. & Merriman, T. R. An update on the genetics of hyperuricaemia and gout. *Nat. Rev. Rheumatol.* **14**, 341–353 (2018).
33. Terkeltaub, R. A. Clinical practice. Gout. *N. Engl. J. Med.* **349**, 1647–1655 (2003).
34. Smith, E. et al. The global burden of gout: estimates from the Global Burden of Disease 2010 study. *Ann. Rheum. Dis.* **73**, 1470–1476 (2014).
35. Fernstrom, J. D. & Fernstrom, M. H. Tyrosine, phenylalanine, and catecholamine synthesis and function in the brain. *J. Nutr.* **137**, 1539S–1547S (2007).
36. Russo, P. A., Mitchell, G. A. & Tanguay, R. M. Tyrosinemia: a review. *Pediatr. Dev. Pathol.* **4**, 212–221 (2001).
37. Levine, R. J. & Conn, H. O. Tyrosine metabolism in patients with liver disease. *J. Clin. Invest.* **46**, 2012–2020 (1967).
38. D'Andrea, G. et al. Study of tyrosine metabolism in eating disorders. Possible correlation with migraine. *Neurol. Sci.* **29**, S88–S92 (2008).
39. Capuron, L. et al. Chronic low-grade inflammation in elderly persons is associated with altered tryptophan and tyrosine metabolism: role in neuropsychiatric symptoms. *Biol. Psychiatry* **70**, 175–182 (2011).
40. Itoh, S. & Nakayama, T. Amino acids in human sweat. *Jpn. J. Physiol.* **2**, 248–253 (1952).
41. Liappis, N., Kelderbacher, S. D., Kessler, K. & Bantzer, P. Quantitative study of free amino acids in human eccrine sweat excreted from the forearms of healthy trained and untrained men during exercise. *Eur. J. Appl. Physiol. Occup. Physiol.* **42**, 227–234 (1979).
42. Reeder, J. T. et al. Waterproof, electronics-enabled, epidermal microfluidic devices for sweat collection, biomarker analysis, and thermography in aquatic settings. *Sci. Adv.* **5**, eaau6356 (2019).
43. Nyein, H. Y. Y. et al. A wearable microfluidic sensing patch for dynamic sweat secretion analysis. *ACS Sens.* **3**, 944–952 (2018).
44. Imani, S. et al. A wearable chemical–electrophysiological hybrid biosensing system for real-time health and fitness monitoring. *Nat. Commun.* **7**, 11650 (2016).
45. Ye, R., James, D. K. & Tour, J. M. Laser-induced graphene. *Acc. Chem. Res.* **51**, 1609–1620 (2018).
46. Lin, J. et al. Laser-induced porous graphene films from commercial polymers. *Nat. Commun.* **5**, 5714 (2014).
47. Li, G., Mo, X., Law, W.-C. & Chan, K. C. Wearable fluid capture devices for electrochemical sensing of sweat. *ACS Appl. Mater. Interfaces* **11**, 238–243 (2018).
48. Harvey, C. J., LeBouf, R. F. & Stefaniak, A. B. Formulation and stability of a novel artificial human sweat under conditions of storage and use. *Toxicol. In Vitro* **24**, 1790–1796 (2010).
49. Shao, Q., Liu, G., Teweldebrhan, D. & Balandin, A. A. High-temperature quenching of electrical resistance in graphene interconnects. *Appl. Phys. Lett.* **92**, 202108 (2008).
50. Snakenborg, D., Klank, H. & Kutter, J. P. Microstructure fabrication with a CO₂ laser system. *J. Micromech. Microeng.* **14**, 182–189 (2004).

Publisher's note Springer Nature remains neutral with regard to jurisdictional claims in published maps and institutional affiliations.

© The Author(s), under exclusive licence to Springer Nature America, Inc. 2019

Methods

Materials and reagents. UA, L-tyrosine, silver nitrate, iron chloride (III), dopamine hydrochloride, choline chloride, creatinine, pantothenic acid calcium salt, citrulline, pyridoxine and lactic acid were purchased from Alfa Aesar. Sodium thiosulfate pentahydrate, sodium bisulfite, tryptophan, leucine, alanine, isoleucine, methionine, valine, lysine, thiamine hydrochloride and serine were purchased from Sigma Aldrich. Potassium ferricyanide (III) was purchased from Acros Organics. Acetic acid, sodium acetate, sodium chloride, urea, L-ascorbic acid and dextrose (D-glucose) anhydrous, glycine, arginine, inositol, ornithine, aspartic acid, threonine, histidine, riboflavin, creatine, phenylalanine, nicotinic acid, folic acid and glutamic acid were purchased from Thermo Fisher Scientific. Medical adhesives were purchased from Adhesives Research. **Polyimide film (75 μm thick) and PET (12 μm and 75 μm thick)** were purchased from DuPont and McMASTER-CARR, respectively. Glassy carbon electrodes were purchased from CH Instruments, screen-printed carbon electrodes were purchased from Metrohm AG and gold electrodes were fabricated on a PET substrate by photolithography followed by 30 nm Cr/100 nm gold deposition via electron-beam evaporation and lift-off in acetone.

Fabrication and characterization of the LEG. For sensor patterning, a polyimide film (DuPont) was attached onto a supporting substrate in a 50-W CO₂ laser cutter (Universal Laser System). The optimized parameters for the chemical sensor were power 6.3%, speed 5.5%, points per inch (PPI) 1,000 and raster mode. After graphene electrodes were scribed, silver was electrodeposited onto one pattern to function as the **reference electrode at -0.2 mA for 100 s using a plating solution** containing 250 mM silver nitrate, 750 mM sodium thiosulfate and 500 mM sodium bisulfite. The physical sensors had their contact pads scribed with the same parameters as the chemical sensors. For the active sensing area of the strain sensor, the optimized parameters were power 0.3%, speed 1.0% (1.4%, 1.2% and 1.0% were described as higher speed, medium speed and lower speed, respectively, in Fig. 3i and Supplementary Fig. 22), PPI 400, vector mode; for the active sensing area of the temperature sensor, the optimized parameters were power 1.5%, speed 11%, PPI 1,000 and vector mode. Scanning electron microscopy (SEM) images were taken with a field emission scanning electron microscope (FEI Sirion). The surface properties of the laser-induced graphene were characterized by X-ray photoelectron spectroscopy (Escalab 250xi, Thermo Fisher Scientific). The Raman spectrum of graphene was recorded using a 532.8-nm laser with an inVia Reflex (Renishaw).

Characterization of the UA and Tyr sensors. **All sensor characterizations were performed in 0.01 M acetate buffer saline (ABS) (pH 4.6 with the addition of 50 mM NaCl) unless otherwise noted. DPV analysis was performed through an electrochemical workstation (CHI 832D).** The detailed parameters were: range, 0–0.9 V; incremental potential, 0.004 V; pulse amplitude, 0.05 V; pulse width, 0.05 s; pulse period, 0.5 s; and sensitivity, 1×10^{-5} A/V. The selectivity study of the LEG was tested in ABS containing physiological concentrations of analytes. The dependence of the sensor response on pH was studied by DPV tests in 0.3× PBS with solution pHs adjusted by lactic acid.

Characterization of the strain and temperature sensors. The temperature sensor characterization was performed on a ceramic hot plate (Thermo Fisher Scientific) (Fig. 3fg and Supplementary Fig. 21). The sensor response was recorded using a parameter analyzer (Keithley 4200A-SCS) and compared with the readings from an infrared thermometer (LASERGRIP 800; Etekcity). The response of the strain sensor was recorded using the parameter analyzer (Keithley 4200A-SCS) in a controlled temperature atmosphere ($23 \pm 1^\circ\text{C}$). The accuracy of the strain sensor for heart rate and respiration rate monitoring was validated on a healthy subject with a commercially available vital-sign monitor (Masimo MightySat; Supplementary Fig. 24). Under repetitive bending under a 0.1% strain for 10,000 cycles (performed using a Lynxmotion AL5D 4DOF Robotic Arm), the mechanical deformation effect on LEG-based electrode was evaluated (Supplementary Fig. 25).

Fabrication and characterization of microfluidic channels. **A double-sided medical adhesive was attached to a substrate in the above-mentioned laser cutter. One layer of medical adhesive was cut through to make the channels and the reservoir, and another layer of medical adhesive was used to interface skin with inlets.** The cylindrical reservoir has a radius of 2.13 mm, a thickness of 140 μm (medical tape) and its volume can thus be calculated as $\sim 2 \mu\text{l}$. The microfluidic channels have a depth of 140 μm and a width of 175 μm . Between two layers lies a thin (12 μm) and transparent PET film. The optimized laser cutter parameters were power 1%, speed 1.5%, PPI 1,000 for reservoir outline and channels, and power 2%, speed 1%, PPI 1,000 for inlet outlines, all in vector mode. The sweat rates were measured via optical image analysis on the basis of the photographs of a microfluidic patch taken sequentially on the different body parts of the subjects. The estimated sweat rates were calculated by the sweat volume changes divided by the time intervals. For Fig. 4f, black dye was dropped in the reservoir, and a transparent 75- μm PET film was used instead of the polyimide layer to prepare the microfluidics for better visibility. An assembled flow patch was attached onto a subject's arm after an iontophoresis session implemented using a Model 3700

Macroduct Sweat Collection System. The flow tests were done with a syringe pump (Thermo Fisher Scientific, 78-01001) and set concentrations of UA and Tyr in ABS. The DPV data were wirelessly transmitted to a laptop computer and automatically converted to concentration via custom-developed software.

Refreshing time analysis and simulations. A ballpark estimate of the concentration refreshing time T_c can be obtained by considering the mass balance of a standard well-mixed model: $dC/dt + (C - C_i)Q/V_r = 0$, where C_i and Q denote, respectively, the new solute concentration and total flow rate into the reservoir, and V_r represents the reservoir volume. This simple ordinary differential equation can be solved analytically to obtain the solute concentration in the reservoir as a function of time t , $C(t) = C_i - (C_i - C_0)e^{-Qt/V_r}$, where C_0 is the initial concentration in the reservoir. Hence, the refreshing time taken for the reservoir to reach a concentration of kC_i can be readily calculated as $T_c = \frac{V_r}{Q} \ln \frac{1-C_0/C_i}{1-k}$. For an experimentally measured sweat rate of $Q = 1.5 \mu\text{l min}^{-1}$ and concentration change from $C_0 = 20 \mu\text{M}$ to $C_i = 80 \mu\text{M}$, we estimate that the designed reservoir volume $V_r = 2 \text{mm}^3$ leads to a refreshing time $T_c \approx 2.7 \text{min}$ to reach $k = 90\%$ of the new concentration. This simple analysis provides an order of magnitude estimate of the required refreshing time by assuming perfect mixing. To obtain more realistic estimates, a three-dimensional model was created with the same geometry of the device. The mass transport process was simulated using a finite-element software COMSOL Multiphysics by numerically solving the Stokes equation for an incompressible flow

$$\nabla p = \mu \nabla^2 \mathbf{v}, \quad \nabla \cdot \mathbf{v} = 0$$

coupled with the convection-diffusion equation

$$\frac{\partial C}{\partial t} + \mathbf{v} \cdot \nabla C = D \nabla^2 C$$

Here p and \mathbf{v} denote, respectively, pressure and flow velocity, whereas μ and D denote, respectively, solvent viscosity and solute diffusivity. The Stokes equation is applicable here because the Reynolds number is on the order of 10^{-2} for this microfluidic device. The solute concentration in the chamber is tracked by computing the average concentration over the bottom surface of the chamber. A flow rate of $0.15 \mu\text{l min}^{-1}$ is prescribed at each inlet, with the no-slip boundary condition on all channel walls. The simulated refreshing time as a function of the number of inlets is displayed in Fig. 4c. The refreshing time decreases as the number of inlets increases; for ten inlets with a total inlet flow rate of $1.5 \mu\text{l min}^{-1}$, the simulated 90% refreshing time is $\sim 2.5 \text{min}$, slightly less than the ballpark estimate on the basis of perfect mixing ($\sim 2.7 \text{min}$). In Fig. 4d, the time evolution of the average concentration under different total inlet flow rates is displayed. In Fig. 4e, the concentration distribution over the bottom surface of the chamber is displayed at different time instances. Similarly, numerical simulation was performed on the basis of the actual design of the microfluidic module used in this work (Supplementary Fig. 27).

Signal conditioning, processing and wireless transmission. At the core of the system lied an STM32L432 ultralow-power ARM Cortex-M4 32-bit microcontroller with a built-in 12-bit ADC (Fig. 1e). The microcontroller was programmed with the ST-link/v2 in-circuit debugger and programmer. For a DPV scan, the microcontroller controlled the DAC8552 digital-to-analog converter through the serial peripheral interface (SPI) protocol to output a steady reference potential for the reference electrode, and a dynamic working potential for the working electrode. A fourth-order low-pass filter further stabilized the reference potential. **The analog circuitry for the filter, potentiostat interface and TIA are shown in Supplementary Fig. 7.** The resulting current through the working electrode was amplified and converted to voltage by the TIA, then read by the ADC peripheral of the microcontroller. The 12-bit ADC had a high sample rate of five million samples per second, allowing precise and time-accurate measurements by taking averages. The default incremental potential of the DPV scan is 0.004 V unless otherwise noted, which leads to a scan cycle of 90 s. The potential steps could be increased to obtain short scan cycles (Supplementary Figs. 17 and 30). The microcontroller was also able to measure the resistance of the vital-sign sensors through voltage divider circuits and the built-in ADC. The acquired multimodal data were wirelessly transmitted via Bluetooth to the user device and further analyzed via custom-developed software. As the output of the electronic system is electrical potential, the wirelessly collected raw signals were plotted in mV in the figures.

Power delivery. The entire system operated at 3.3 V, enabling a simple and efficient design. A single LD39050 voltage regulator converted the power from a 3.7 V Li-ion battery to a stable 3.3 V. During data acquisition and transmission, the FPCB drew 27 mA from the 3.7 V Li-ion battery. Using a 400-mAh battery, the device could perform approximately 592 full cycles of the 90-s DPV measurements.

Human subject recruitment. The validation and evaluation of the sweat sensor were performed using human subjects in compliance with all the ethical regulations under a protocol (ID 19-0892) that was approved by the Institutional Review Board (IRB) at California Institute of Technology. The participating

subjects (age range 18–65) were recruited from the California Institute of Technology campus and the neighboring communities through advertisement. All subjects gave written informed consent before participation in the study.

On-body system validation. To validate the multimodal sweat sensor, we conducted constant-load cycling exercise on five physically trained and five physically untrained subjects (all male). The trained subjects (athletes from California Institute of Technology sport teams) exercised regularly for at least 9 h per week while the untrained subjects had an average of 1 h of exercise per week. The subjects reported to the lab with overnight fasting and were given a standardized protein drink (Fairlife, Core Power Elite). Two hours after the protein consumption, the subjects' foreheads and necks were cleaned with alcohol swabs and gauze before the sensor patches were placed on the body. A stationary exercise bike (Kettler Axos Cycle M-LA) was used for cycling trials. The subjects cycled at 60 rpm for 40 min. During the on-body trial, the data from the sensor patches were wirelessly sent to the user interface via Bluetooth. When the subjects started biking, the sensor system continuously acquired and transmitted physical sensor data at a rate of 10 Hz. Every minute, the electronic system initiated a transient voltage bias between the reference and working electrodes. If the bias triggered a current above an experimentally determined threshold, the system would start the first 90-s DPV scan. The DPV scan was repeated every 5 min until the subject stopped biking. After being calibrated using simultaneously collected skin temperature information in the preprogrammed microcontroller (Fig. 3l), the acquired molecular data were wirelessly transmitted via Bluetooth to the user device, and further converted to the concentration levels on the basis of the calibration curves in Fig. 5e,f. The respiration rate was calculated through spectral analysis by performing fast Fourier transform on the respiration sensor data (Supplementary Fig. 32). The frequency corresponding to the largest amplitude in the frequency spectrum was converted to breaths per minute. Meanwhile sweat samples were collected periodically from the forehead and neck of the subjects using centrifuge tubes and then centrifuged at 6,000 rpm for 15 min. The sweat samples were then frozen at -20°C for further testing and validation via electrochemical test with the LEG-CS, HPLC analysis and the colorimetric assay kits. For the tyrosine supplementation study, the subject consumed 1.5 g tyrosine 6 min after an iontophoresis session implemented using a Model 3700 Macroduct Sweat Collection System. Over a 50-min period, the subject's sweat was sampled periodically and analyzed by the sensor patch while the sweat flow rate was estimated by the sweat volume in each sampling period (Supplementary Fig. 37).

HPLC analysis for sensor validation and sample analysis. HPLC tests of UA and Tyr were done on HP Agilent 1100 HPLC using an Agilent Eclipse XDB-C18 $5\ \mu\text{m}\ 3 \times 250\ \text{mm}$ column. Tests of UA and Tyr were done with gradient methods and the gradient profiles are shown in Supplementary Tables 3 and 4. Detection wavelengths for UA and Tyr were 245 nm and 274 nm, respectively. Retention times were $\sim 9\ \text{min}$ and $\sim 4\ \text{min}$ for UA and Tyr, respectively. Sweat samples and serum samples were diluted to around $400\ \mu\text{l}$, both with water. The selectivity study of the HPLC was performed by spiking a constant concentration of UA or Tyr with different sweat analytes with concentrations listed in Supplementary Table 2.

Colorimetric assays for sensor validation and sample analysis. For UA analyses, the QuantiChrom Uric Acid Assay kit (BioAssay Systems) was used for the determination of UA levels in sweat. The kit quantifies UA in the sample by utilizing 2,4,6-tripyridyl-s-triazine, which forms a blue-colored complex with iron in the presence of UA. Five microliters of samples and standard solutions were transferred in triplicate wells of a clear-bottom 96-well plate, followed by addition of $200\ \mu\text{l}$ of working reagents. The microplate was incubated for 30 min at room temperature. The absorbance at a wavelength of 620 nm was measured using a microplate photometer (Multiskan FC) and the concentration of uric acid was calculated according to the standard curve ($n=3$). Standard kits and solutions were kept at 4°C and -20°C unless otherwise used. For Tyr analyses, the Tyrosine Assay kit (Cell Biolabs) was used for the determination of Tyr levels in sweat. The kit quantifies the colorimetric intermediate formed via enzymatic oxidation of Tyr. Fifty microliters of samples and standard solutions were transferred in triplicate wells of a clear-bottom 96-well plate, followed by addition of $50\ \mu\text{l}$ of working reagents. The microplate was incubated for 10 min at room temperature on an orbital shaker. The absorbance at a wavelength of 450 nm was measured using a microplate photometer (Multiskan FC) and the concentration of tyrosine was calculated according to the standard curve ($n=3$).

Human trials for gout management. To evaluate the sensor performance toward gout management, a purine-rich diet study was performed on both healthy male and female subjects (Fig. 6b–e and Supplementary Fig. 39). The subjects reported to the lab after overnight fasting. Fresh capillary blood samples were collected using a finger-prick approach before the exercise. After cleaning the fingertip with alcohol wipe and allowing it to air dry, the skin was punctured with CareTouch lancing device. Samples were collected with centrifuge tubes after wiping off the first drop of blood with gauze. After the 90-min standardized clotting procedure

finished, serum was separated by centrifuging at 6,000 rpm for 15 min, and instantly stored at -20°C for HPLC analysis. A 20-min constant-load cycling exercise was immediately conducted on the subjects after the blood collection with the sweat information collected by the sensor patch from the forehead. The subjects were then given a purine-rich diet (250 g of canned sardines) followed by a 2-h rest. The blood collection and the cycling trial were then repeated. The plotted data for this study are based on the first two successive complete DPV measurements. To further characterize the sweat UA sensing, six patients with gout, four subjects with hyperuricemia (without history of gout attack) and five healthy subjects were recruited (Fig. 6f). It should be noted that all of the six patients with gout (three currently under urate-lowering therapy, three not on any medical therapy) didn't receive any urate-lowering medication for at least 10 h ahead of the study. The sweat samples and blood samples were collected 2 h after their regular lunch and tested by the sensor patches and HPLC, respectively (same procedure as the after meal test in the meal challenge study). During the on-body test, sweat samples were collected periodically from the subjects using centrifuge tubes and then frozen at -20°C for further sensor validation via HPLC analysis. For dynamic monitoring of UA before and after purine intake (Fig. 6g), a healthy subject underwent a finger-prick blood collection followed by a 20-min cycling test after overnight fasting, then consumed canned sardines. The blood collection and sweat test were repeated periodically every hour until 6 h after the intake. The collected blood samples were analyzed with HPLC. To investigate the medication influence on serum and sweat UA levels, a patient with gout underwent the sweat and blood sample tests on two days: on one day the patient received urate-lowering medication (allopurinol) 2 h before the test and on the other day the patient did not take medication for 24 h before the test. The sweat samples and blood samples were collected 2 h after their regular lunch and tested by the sensor patches and HPLC, respectively (same procedure as the after meal test in the meal challenge study). The correlation plot in Fig. 6h was based on data obtained from 15 subjects (including six patients with gout). The Pearson correlation coefficient was acquired through linear regression in Origin 2018 ($n=46$).

Reporting Summary. Further information on research design is available in the Nature Research Reporting Summary linked to this article.

Data availability

The data that support the plots within this paper and other findings of this study are available from the corresponding author upon request.

Code availability

The custom code used to program microcontroller is available from the corresponding author upon request.

Acknowledgements

This work was supported by a California Institute of Technology Startup grant, the Rothenberg Innovation Initiative (RI²) program, the Carver Mead New Adventures Fund and an American Heart Association grant 19TPA34850157 (all to W.G.). Y.S., X.B. and M.W. acknowledge the China Scholarship Council (CSC) for financial support. J.T. was supported by the National Science Scholarship (NSS) from the Agency of Science Technology and Research (A*STAR) Singapore. We gratefully acknowledge critical support and infrastructure provided for this work by the Kavli Nanoscience Institute and Jim Hall Design and Prototyping Lab at Caltech, and we gratefully thank M. Hunt and B. Dominguez for their help. This project benefited from the use of instrumentation made available by the Caltech Environmental Analysis Center and we gratefully acknowledge guidance from N. Dalleska. We also thank Z. Wang for valuable inputs in patch pattern design.

Author contributions

W.G. and Y.Y. initiated the concept. W.G., Y.Y., Y.S., X.B., T.K.H. and Z.L. designed the experiments; Y.Y., Y.S., X.B. and J.M. led the experiments and collected the overall data; O.S.P., L.Z. and Y.Y. performed the flow simulation and modeling; J.M. performed the circuit design and test; M.W., J.T. and A.K. contributed to sensor characterization and validation; W.G., Y.Y., Y.S., X.B., J.M., O.S.P., L.Z. and H.Z. contributed the data analysis and co-wrote the paper. All authors provided the feedback on the manuscript.

Competing interests

The authors declare no competing interests.

Additional information

Supplementary information is available for this paper at <https://doi.org/10.1038/s41587-019-0321-x>.

Correspondence and requests for materials should be addressed to W.G.

Reprints and permissions information is available at www.nature.com/reprints.

Reporting Summary

Nature Research wishes to improve the reproducibility of the work that we publish. This form provides structure for consistency and transparency in reporting. For further information on Nature Research policies, see [Authors & Referees](#) and the [Editorial Policy Checklist](#).

Statistics

For all statistical analyses, confirm that the following items are present in the figure legend, table legend, main text, or Methods section.

n/a Confirmed

- The exact sample size (n) for each experimental group/condition, given as a discrete number and unit of measurement
- A statement on whether measurements were taken from distinct samples or whether the same sample was measured repeatedly
- The statistical test(s) used AND whether they are one- or two-sided
Only common tests should be described solely by name; describe more complex techniques in the Methods section.
- A description of all covariates tested
- A description of any assumptions or corrections, such as tests of normality and adjustment for multiple comparisons
- A full description of the statistical parameters including central tendency (e.g. means) or other basic estimates (e.g. regression coefficient) AND variation (e.g. standard deviation) or associated estimates of uncertainty (e.g. confidence intervals)
- For null hypothesis testing, the test statistic (e.g. F , t , r) with confidence intervals, effect sizes, degrees of freedom and P value noted
Give P values as exact values whenever suitable.
- For Bayesian analysis, information on the choice of priors and Markov chain Monte Carlo settings
- For hierarchical and complex designs, identification of the appropriate level for tests and full reporting of outcomes
- Estimates of effect sizes (e.g. Cohen's d , Pearson's r), indicating how they were calculated

Our web collection on [statistics for biologists](#) contains articles on many of the points above.

Software and code

Policy information about [availability of computer code](#)

Data collection

Mbed was used to program microcontroller. CH Instrument was used for off-body sensor data collection. Comsol was used for simulations.

Data analysis

Origin 2018 was used to analyze all data, plot the data and calculate the statistical parameters. FFT analysis of the respiration sensor data using the built-in code in MATLAB R2018b

For manuscripts utilizing custom algorithms or software that are central to the research but not yet described in published literature, software must be made available to editors/reviewers. We strongly encourage code deposition in a community repository (e.g. GitHub). See the Nature Research [guidelines for submitting code & software](#) for further information.

Data

Policy information about [availability of data](#)

All manuscripts must include a [data availability statement](#). This statement should provide the following information, where applicable:

- Accession codes, unique identifiers, or web links for publicly available datasets
- A list of figures that have associated raw data
- A description of any restrictions on data availability

The data that support the plots within this paper and other findings of this study are available from the corresponding author upon request.

Field-specific reporting

Please select the one below that is the best fit for your research. If you are not sure, read the appropriate sections before making your selection.

- Life sciences Behavioural & social sciences Ecological, evolutionary & environmental sciences

Life sciences study design

All studies must disclose on these points even when the disclosure is negative.

Sample size	10 subjects (five trained and five untrained) were involved for on-body system validation; 1 subject for tyrosine supplement study; 15 subjects were involved in the purine study. Sample sizes were chosen on the basis of literature standards for proof-of-concept experiments. There is no self-selection biases or other biases.
Data exclusions	No data exclusion.
Replication	All attempts at replication were successful when following the device fabrication process described in the paper.
Randomization	The device was fabricated with same process and was tested in all participants under same conditions. Randomization was therefore not relevant to the study.
Blinding	Not relevant, because a blinding process wouldn't influence the sampling result

Reporting for specific materials, systems and methods

We require information from authors about some types of materials, experimental systems and methods used in many studies. Here, indicate whether each material, system or method listed is relevant to your study. If you are not sure if a list item applies to your research, read the appropriate section before selecting a response.

Materials & experimental systems

Methods

n/a	Involvement
<input checked="" type="checkbox"/>	<input type="checkbox"/> Antibodies
<input checked="" type="checkbox"/>	<input type="checkbox"/> Eukaryotic cell lines
<input checked="" type="checkbox"/>	<input type="checkbox"/> Palaeontology
<input checked="" type="checkbox"/>	<input type="checkbox"/> Animals and other organisms
<input type="checkbox"/>	<input checked="" type="checkbox"/> Human research participants
<input checked="" type="checkbox"/>	<input type="checkbox"/> Clinical data

n/a	Involvement
<input checked="" type="checkbox"/>	<input type="checkbox"/> ChIP-seq
<input checked="" type="checkbox"/>	<input type="checkbox"/> Flow cytometry
<input checked="" type="checkbox"/>	<input type="checkbox"/> MRI-based neuroimaging

Human research participants

Policy information about [studies involving human research participants](#)

Population characteristics	For on-body system validation, physically trained and untrained subjects (age range 18-65, male) were recruited. The trained subjects (athletes from Caltech sport teams) exercised regularly for at least 9 h per week while the untrained subjects had an average of 1 h of exercise per week. For purine study, six male patients with gout, four male subjects with hyperuricemia, and five healthy subjects (four male and one female) were recruited (age range 18-65).
Recruitment	The participating subjects (trained and untrained subjects, healthy and hyperuricemic subjects, gout patients), were recruited from Caltech campus, UCLA hospital and the neighboring communities through advertisement by posted notices, word of mouth, and email distribution. There were no self-selection biases or other biases.
Ethics oversight	California Institute of Technology

Note that full information on the approval of the study protocol must also be provided in the manuscript.